Exploring the Capability of ALOS PALSAR L-Band Fully Polarimetric Data for Land Cover Classification in Tropical Environments

Rogério Galante Negri, Luciano Vieira Dutra, Corina da Costa Freitas, and Dengsheng Lu

***Abstract*—Among different applications using synthetic aperture radar (SAR) data, land cover classification of rain forest areas has been investigated. Previous results showed that L-band is more appropriate for such applications. However, SAR images have limited discriminability for mapping large sets of classes compared with optical imagery. The objective of this study was to carry out an analysis about the discriminative capability of an L-band fully polarimetric SAR complex image, compared to the possible subsets of polarizations in amplitude/intensity, for mapping land cover classes in Amazon regions. Two case studies using ALOS PALSAR L-band fully polarimetric images over Brazilian Amazon regions were considered. Several thematic classes, organized into scenarios, were considered for each case study. These scenarios represent distinct classification tasks with variated complexities. Performing a simultaneous analysis of different scenarios is a distinct way to assess the discriminative capability offered by a particular image. A methodology to organize thematic classes into scenarios is proposed in this study. The maximum likelihood classifier (MLC), with specific distributions for SAR data, and support vector machine were considered in this study. The iterated conditional modes algorithm was adopted to incorporate the contextual information in both methods. Considering a kappa coefficient equal to 0.8 as an acceptable minimum, the experiments show that none subset of polarization or fully polarimetric image allows performing discrimination between forest and regeneration types; single-polarized HV data provide acceptable results when the classification problem deals with the discrimination of a few classes; depending on the classification scenario, the dual-polarized HH+HV image produces similar results when compared to multipolarized (i.e., HH+HV+VV) data; in turn, if the MLC method is adopted, multipolarized data may produce close or statistically indifferent classification results compared to those produced with the use of fully polarimetric data.**

***Index Terms*—Amazon, assessment, image classification, polarimetric synthetic aperture radar (PolSAR), scenarios, synthetic aperture radar (SAR).**

Manuscript received January 29, 2016; revised May 19, 2016; accepted July 21, 2016. Date of publication August 23, 2016; date of current version November 30, 2016. This work was supported in part by FAPESP under Grant 2014/14830-8 and Grant 2007/02139-5, in part by UNESP/PROPe under Grant 2016/1163, in part by CNPq under Grant 307666/2011-5, and in part by NSF under Grant BCS0850615.

R. G. Negri is with the Departamento de Engenharia Ambiental, Universidade Estadual Paulista, São José dos Campos 12245-000, Brazil (e-mail: rogerio.negri@ict.unesp.br).

L. V. Dutra and C. C. Freitas are with Divisão de Processamento de Imagens, Instituto Nacional de Pesquisas Espaciais, São José dos Campos, 12227-010, Brazil (e-mail: dutra@dpi.inpe.br; corina@dpi.inpe.br).

D. Lu is with Center for Global Change and Earth Observations, Michigan State University, East Lansing, MI 48824 USA (e-mail: ludengsh@msu.edu).

Color versions of one or more of the figures in this paper are available online at http://ieeexplore.ieee.org.

Digital Object Identifier 10.1109/JSTARS.2016.2594133

I. Introduction

In tropical regions, atmospheric conditions, like the extensive cloud cover, are obstacles for acquiring images with optical sensors, which are the main source for large area environmental studies. Remote platforms with synthetic aperture radar (SAR) sensors have been developed as an alternative for having an almost-all-weather monitoring data source.

An SAR sensor has its specific applications. Examples of forestry applications using SAR data are related to large area biomass estimation [1]–[3], digital elevation model estimation using interferometry [4], [5], tree height estimation [6], [7], deforestation detection [8], and change detection [9], [10].

Land cover classification of forestry areas is another important application where SAR data have been analyzed [11]–[15]. For this application purposes, it was already verified that L-band SAR images are preferable, since they provide a better distinction between forest and other targets, as presented in [13], [16], and [17]. However, as observed in [13] and [18], generally, SAR images do not have the capability for fine land cover classification, for example, to separate different types of forest and secondary successions.

An alternative to improving the target separability, and consequently, the classification accuracy, is to adopt polarimetric SAR (PolSAR) sensors. Compared to the conventional SAR, which acquires amplitude information in different polarizations, PolSAR sensors are able to obtain the amplitude, phase, and orientation of the electromagnetic waves reflected from targets. Fully PolSAR sensors are polarimetric sensors able to record the amplitude and phase information of the waves in all possible polarization combinations, with respect to an adopted basis, for transmission and reception. Different techniques for fully PolSAR data classification have been developed and adopted in diverse applications, for example, the pioneer method proposed in [19] for unsupervised classification based on eigenvalue analysis of the coherency matrix and the study presented in [20], where the use of specific probability density functions developed for polarimetric data in the simple Maximum Likelihood Classifier method was successfully verified.

Despite the availability of SAR and PolSAR images as methods to process such data, investigations comparing how many classes L-band SAR and fully PolSAR data are able to discriminate in land cover classification of rain forest areas have still not been carried out. Under this circumstance, the objective of this study was to systematically assess the classification capability of using fully PolSAR data, in comparison to its subsets of polarizations, for mapping land cover classes in a moist tropical forest region. This objective is summarized in three main questions. 1) Is it worthwhile to use fully PolSAR data instead of the three polarizations (i.e., no phase information)? 2) For each feature space dimensionality, what is/are the best polarization or polarizations? 3) What are the main characteristic of the classes that can usually be satisfactorily discriminated (*ad hoc* considering a minimum kappa coefficient of agreement of 0.8 acceptable) when using from one to three SAR polarizations or fully PolSAR data.

For the purposes of this research, two case studies using fully PolSAR L-band images acquired with ALOS PALSAR in April 2007 and March 2009 over the Tapajós National Forest and the Altamira region, located in the Brazilian Amazon, were considered. The maximum likelihood classifier (MLC), with specific statistical distributions for SAR and fully PolSAR images, and the support vector machine (SVM) methods were adopted to perform the classifications. Classification results obtained from both methods were regularized using the iterated conditional modes (ICM) algorithm. In order to provide a more general assessment about the discriminative capability of fully PolSAR images as polarized data, several class configurations, called scenarios, were considered. These scenarios were determined by a methodology proposed in this paper.

This paper was organized as follows: Section II presents concepts regarding the statistical modeling and SAR image classification. Section III presents details about the data, the scenario construction procedure, the experiment design, the obtained results, and discussions. The conclusions of this study are presented in Section IV.

II. Theoretical Background

A. Statistical SAR Image Modeling

A signal measurement obtained by a fully PolSAR sensor is usually represented by $\mathbf{z}^T = (S_{hh}\ S_{hv}\ S_{vh}\ S_{vv})$, known as a complex scattering vector. The components of $\mathbf{z}$ are complex numbers that represent the amplitude and phase of a defined linear polarization combination. The polarizations are indicated by the subscripts on the components of $\mathbf{z}$, where, for example, hv denotes the signal recorded with vertical polarization from a signal initially emitted with horizontal polarization. Given the reciprocity of an atmospheric medium, where $S_{hv} = S_{vh}$, the scattering vector is simplified to $\mathbf{z}^T = (S_{hh}\ S_{hv}\ S_{vv})$ [20]. A fixed number n of $\mathbf{z}$ observations, in a neighborhood, are averaged to form the n-looks 3×3 covariance matrix, defined as follows:

$$\mathbf{Z} = \frac{1}{n}\sum_{k=1}^{n} \mathbf{z}(k) \cdot \mathbf{z}^{\star T}(k) = \begin{pmatrix} \mathbf{Z}_{hh} & \mathbf{Z}_{hhhv} & \mathbf{Z}_{hhvv} \\ \mathbf{Z}^{\star}_{hhhv} & \mathbf{Z}_{hv} & \mathbf{Z}_{hvvv} \\ \mathbf{Z}^{\star}_{hhvv} & \mathbf{Z}^{\star}_{hvvv} & \mathbf{Z}_{vv} \end{pmatrix} \quad (1)$$

where $\star$ and T represent the conjugate and transposed operators, respectively. The diagonal elements of $\mathbf{Z}$ are real numbers that represent the intensity of the signal measured on a specific polarization. Nondiagonal elements are complex numbers that contain information about amplitudes and phase differences between two polarizations.

$\mathbf{Z}$ can be modeled using different distributions according to the target texture. Targets with homogeneous, heterogeneous, and extremely heterogeneous textures can lead $\mathbf{Z}$ to have Wishart, K_{Complex} [21], and G^0_{Complex} [20], defined, respectively, by

$$G(\mathbf{Z}; n, h) = \frac{n^{nh}|\mathbf{Z}|^{n-h} e^{-nTr\left(\Sigma^{-1}\mathbf{Z}\right)}}{M(n,h)|\Sigma|^n};\ n, h \in \mathbb{R}_+ \quad (2)$$

$$G(\mathbf{Z}; g, n, h) = \frac{2|\mathbf{Z}|^{n-h}(ng)^{\frac{g+hn}{2}}}{M(n,h)|\Sigma|^n \Gamma(g) Tr\left(\Sigma^{-1}\mathbf{Z}\right)^{\frac{hn-g}{2}}} \cdot \cdot K_{g-hn}\Big(2\sqrt{(ngTr(\Sigma^{-1}\mathbf{Z}))}\Big);\ g, n, h \in \mathbb{R}_+ \quad (3)$$

$$G(\mathbf{Z}; g, n, h) = \frac{\Gamma(hn-g)\left(nTr\left(\Sigma^{-1}z\right) - g\right)^{-(hn-g)}}{-g^g\left(n^{nh}|\mathbf{Z}|^{n-h}\right)^{-1}\Gamma(-g)K(n,h)|\Sigma|^n} - g, n, h \in \mathbb{R}_+ \quad (4)$$

where g, h, n, $|\cdot|$, $(\cdot)^{-1}$, and $Tr(\cdot)$ are real parameters, the number of polarimetric components, the equivalent number of looks, the determinant, inversion, and matricial trace, respectively. $M(n,c) = \pi^{\frac{c(c-1)}{2}} \prod_{k=n-c-1}^{n} \Gamma(k)$, K_{a-qn} is the modified Bessel function of third type and order $a - cn$ and $\Gamma(\cdot)$ is the Euler gamma function. Σ is a complex covariance matrix computed from a set of observations (a set of vectors of type $\mathbf{Z}$). If the amplitude[1] information of one diagonal element of $\mathbf{Z}$ is considered, the Wishart, K_{Complex} and G^0_{Complex} distributions are derived to the square root of gamma [22], $K_{\text{Amplitude}}$ [23], and $G^0_{\text{Amplitude}}$ [24] distributions, respectively, defined by

$$G(Z; n, h) = \frac{2h^n}{\Gamma(n)} Z^{2n-1} e^{-hZ^2};\ Z, n, h \in \mathbb{R}_+ \quad (5)$$

$$G(Z; n, g, h) = \frac{4hnZ}{b\Gamma(g)\Gamma(n)} \sqrt{\left(\frac{gnZ^2}{h}\right)^{g+n-2}} \cdot \cdot K_{g-n}\left(2Z\sqrt{\frac{gn}{h}}\right);\ Z, n, g, h \in \mathbb{R}_+ \quad (6)$$

$$G(Z; n, g, h) = \frac{2n^n \Gamma(n-g) Z^{2n-1}}{h^g \Gamma(n)\Gamma(-g)\left(h + nZ^2\right)^{n-g}} \quad Z, n, -g, h \in \mathbb{R}_+ \quad (7)$$

where g and h are real parameters in these distributions and Z represents the amplitude of the signal.

From a Wishart distribution, the study presented in [25] derives a distribution for a pair of intensities (i.e., two diagonal elements of $\mathbf{Z}$), represented by the vector $\left(Z_1^2, Z_2^2\right)$, with two

[1] Amplitude information is obtained from the square root of the intensity information.

square diagonal elements of $\mathbf{Z}$

$$G\left(Z_1^2, Z_2^2\right) = \frac{n^{n+1}\left(Z_1^2 Z_2^2\right)^{\frac{n-1}{2}} e^{\frac{-n\left(Z_1^2/\mu_1 + Z_2^2/\mu_2\right)}{1-\|\rho\|^2}}}{\left(\mu_1\mu_2\right)^{\frac{n+1}{n}}\Gamma(n)\left(1-\|\rho\|^2\right)\|\rho\|^{n-1}} \cdot I_{n-1}\left(\frac{2n\|\rho\|}{1-\|\rho\|^2}\sqrt{\frac{Z_1^2 Z_2^2}{\mu_1\mu_2}}\right) \quad (8)$$

where μ_1 and μ_2 are the mean values of Z_1^2 and Z_2^2, respectively. $\|\rho\|$ is the norm of a multilook complex correlation coefficient and $I_{n-1}(\cdot)$ is the modified Bessel function of order $n-1$.

Under certain conditions, for example, large n values, multivariate Gaussian distribution to model the amplitude diagonal elements of $\mathbf{Z}$, denoted by $\boldsymbol{Z}$, can be adopted

$$G(\boldsymbol{Z};\mu,\Phi) = \frac{1}{2\pi^{\frac{c}{2}}|\Phi|^{\frac{1}{2}}} e^{-\frac{1}{2}(\boldsymbol{Z}-\mu)\Phi^{-1}(\boldsymbol{Z}-\mu)} \quad (9)$$

where c is the number of elements (polarizations) in $\boldsymbol{Z}$, μ is the mean vector, and Φ is a real covariance matrix computed from a set of observations (a set of $\boldsymbol{Z}$ type vectors).

In this study, images with only the amplitude of one diagonal element of $\mathbf{Z}$ are called single polarized. Dual-polarized images are composed of the intensity of two diagonal elements of $\mathbf{Z}$ and multipolarized images have the amplitudes of all the diagonal elements of $\mathbf{Z}$ as attributes. Images whose pixels contain all the information represented in (1) are referred to as fully polarimetric SAR (fully PolSAR) images.

It is worth mention that the mentioned distributions for fully polarimetric data [Wishart, K_{Complex}, and G^0_{Complex}—(2)–(4)] and single polarized data [square root of gamma, $K_{\text{Amplitude}}$, and $G^0_{\text{Amplitude}}$—(5)–(7)] can be fitted to each one of the classes of interest according to each class's characteristics. No fitting procedure is applied when considering the dual- and multipolarized cases.

B. SAR Image Classification

A classification method may be represented by the function $F:\mathcal{X}\rightarrow\mathcal{Y}$, which assigns elements of attribute space $\mathcal{X}$ to a class $\omega_y \in \Omega = \{\omega_1, \omega_2, \ldots, \omega_c\}$, using label indicator y in $\mathcal{Y} = \{1, 2, \ldots, c\}$, where $c \in \mathbb{N}^*$. Under these conditions, let $\mathbf{x}\in\mathcal{X}$, $y = F(\mathbf{x})$ indicate that $\mathbf{x}$ is assigned to ω_y. The different image classification methods proposed in the literature may be understood as distinct ways of modeling the function F to identify targets in an image $\mathcal{I}$ among a defined set of thematic classes. For methods with supervised learning, available information in a *training set* $\mathcal{D} = \{(\mathbf{x}_l, y_l)\in\mathcal{X}\times\mathcal{Y} : l = 1,\ldots,m\}$, where $m\in\mathbb{N}^*$, is used to model F. The mapping between $\mathcal{X}$ and $\mathcal{Y}$, defined by F, represents the knowledge acquired from observations in $\mathcal{D}$.

The MLC is a supervised method that is usually adopted in remote sensing applications. In this method, considering $P(\mathbf{x}|\omega_k)$ to be the probability distribution of ω_k, for $k = 1,\ldots,c$, estimated from $\mathcal{D}$, the following rule is used to classify the pattern (attribute vector of a given pixel) $\mathbf{x}_i$ in the position/coordinate i of $\mathcal{I}$

$$\mathbf{x}_i \text{ is assigned to } \omega_j \Leftrightarrow j = \underset{k=1,\ldots,c}{\arg\max}\left\{P(\mathbf{x}_i|\omega_k)\right\}. \quad (10)$$

In this study, the probability distribution $P(\mathbf{x}|\omega_k)$ represents one of the functions previously mentioned in Section II-A (i.e., Wishart, K_{Complex}, G^0_{Complex}, $K_{\text{Amplitude}}$, $G^0_{\text{Amplitude}}$, the distribution for pair of intensities proposed in [21], and the multivariate Gaussian), chosen for convenience to model the elements of ω_k.

The classification of an image $\mathcal{I}$ is obtained by applying the rule (10) to the attribute vector of each pixel of this image. One way to improve the classifications obtained from the MLC method is to incorporate contextual information using the ICM algorithm [26]. This combination of methods is denoted by MLC/ICM. Based on concepts associated with Markovian random fields, the ICM algorithm basically consists of solving the following maximization problem [27]:

$$\mathbf{x}_i \text{ is assigned to } \omega_j \Leftrightarrow j = \underset{k=1,\ldots,c}{\arg\max}\left\{P(\mathbf{x}_i|\omega_k) + \right. \left. + \sum_{\eta\in W}\left(\beta\sum_{t\in\mathcal{V}(i)}\left(1-\delta(y_i, y_t)\right)\right)\right\} \quad (11)$$

where β is a parameter that weights the influence of neighboring pixels, η is a clique[2] that contains i which belongs to the set of cliques W, $\mathcal{V}(i)$ is the coordinate set of neighboring pixels of i, and $\delta(\cdot,\cdot)$ represents the Kronecker delta function.[3]

To classify SAR images, the term $P(\mathbf{x}_i|\omega_k)$ in (11) may be replaced by the distribution models mentioned in Section II-A. Under these conditions, the MLC/ICM method takes specific characteristics of the SAR images into consideration in the contextual classification process.

An SVM is one example of a conventional method that can be used for SAR image classification. This method has received great attention in recent years due to its excellent generalization ability, data distribution independence, and robustness with respect to the Hughes phenomenon [28]. The main objective of the SVM consists of finding a binary separating hyperplane between training samples with the largest margin. The separating hyperplane is the geometric location where the following linear function is equal to zero:

$$f(\mathbf{x}) = \langle\mathbf{w},\mathbf{x}\rangle + b \quad (12)$$

where $\mathbf{w}$ represents the orthogonal vector to the hyperplane $f(\mathbf{x}) = 0$, $b/\|\mathbf{w}\|$ is the distance from the hyperplane to the origin, and $\langle\cdot,\cdot\rangle$ denotes the inner product. Based on the training set $\mathcal{D} = \{(\mathbf{x}_i, y_i)\in\mathcal{X}\times\mathcal{Y} : i = 1,\ldots,m\}$, where $\mathcal{Y} = \{-1,+1\}$, the parameters of (12) are obtained from the

[2]A clique of an undirected graph $\mathcal{G} = (\mathcal{A},\mathcal{B})$ is a set of vertices $\bar{\mathcal{A}}\subseteq\mathcal{A}$ such for all $i, j\in\bar{\mathcal{A}}$, there is an edge between i and j.

[3]$\delta(i,j) = \begin{cases} 1, & \text{if } i = j \\ 0, & \text{if } i \neq j. \end{cases}$

following quadratic optimization problem [29]:

$$\min_{\lambda} \sum_{i=1}^{m} \lambda_i - \frac{1}{2} \sum_{i=1}^{m} \sum_{j=1}^{m} \lambda_i \lambda_j y_i y_j \langle \mathbf{x}_i, \mathbf{x}_j \rangle$$
$$\text{subject to: } \begin{cases} 0 \leq \lambda_i \leq C, i = 1, \ldots, m \\ \sum_{i=1}^{m} \lambda_i y_i = 0 \end{cases} \tag{13}$$

where λ are Lagrangian multipliers upper bounded by C, a real parameter that acts as a penalty for misclassifications. It is worth mentioning that in the apreviously presented formulation, a class indicator $y_i = +1$ defines $\mathbf{x}_i \in \omega_1$ as $y_i = -1$ defines $\mathbf{x}_i \in \omega_2$. This definition differs from that presented at the beginning of this subsection for the convenience of SVM formalization.

A set of support vectors (SV) is defined by the pattern $\mathbf{x}_i$ such that $\lambda_i \neq 0$. From this optimization, the parameters $\mathbf{w}$ and b may be computed by the following:

$$\mathbf{w} = \sum_{\forall \mathbf{x}_i \in \text{SV}} y_i \lambda_i \mathbf{x}_i \tag{14}$$

$$b = \frac{1}{\#\text{SV}} \left(\sum_{\mathbf{x}_i \in \text{SV}} y_i + \sum_{\mathbf{x}_i \in \text{SV}} \sum_{\mathbf{x}_j \in \text{SV}} \lambda_i \lambda_j y_i y_j \langle \mathbf{x}_i, \mathbf{x}_j \rangle \right). \tag{15}$$

where $\#$ is the cardinality operator.

When $f(\mathbf{x})$ is determined, $\mathbf{x}_i$ is assigned to ω_1 if $f(\mathbf{x}_i) \geq 0$ or to ω_2 when $f(\mathbf{x}_i) < 0$. To apply this method to problems involving more than two classes, the use of multiclass strategies is necessary, and one-against-all (OAA) is a commonly adopted multiclass strategy [29]. The inner product of (12), as in the quadratic optimization problem (13), can be replaced by kernel functions $K(\mathbf{x}_i, \mathbf{x}_j)$. The polynomial function, defined by $K(\mathbf{x}_i, \mathbf{x}_j) = (\langle \mathbf{x}_i, \mathbf{x}_j \rangle + 1)^q$, where $q \in \mathbb{Z}_+$ and the radial basis function, written as $K(\mathbf{x}_i, \mathbf{x}_j) = e^{-\gamma \|\mathbf{x}_i - \mathbf{x}_j\|^2}$, with $\gamma \in \mathbb{R}_+$ are typical examples of kernel functions.

To contextualize SVM classifications using the ICM algorithm, the function (12) must be interpreted as a probabilistic distribution $P(\mathbf{x}_i | \omega_k)$. A method capable of this interpretation is presented in [30]. The combination of the SVM and ICM is denoted by SVM/ICM.

III. Experiments

In this section, experiments were carried out with the objective of systematically assessing the classification capability of full PolSAR data, in comparison to different combinations of amplitude/intensity polarizations on this data, for mapping land cover classes in moist tropical forest regions. The classification methods (MLC/ICM and SVM/ICM) discussed in Section II-B were adopted.

For this purpose, we considered two case studies using an ALOS PALSAR L-band full polarimetric image over two distinct Amazon areas. The comparison between results was made using the kappa coefficient [31] and hypothesis tests. Furthermore, several class configurations, called scenarios, were considered in the analysis. Such scenarios were determined by a methodology proposed in this paper.

More details about the data used in the experiments are presented in Section III-A. The proposed methodology for the definition of scenarios is exposed in Section III-B. A description of the experiment design is provided in Section III-C. Results and discussions are presented in Section III-D.

A. *Description of the Data*

Two study areas are considered in the experiments. The first area is located in the south of Santarém, Pará, Brazil, near to the Tapajós National Forest. The other area, also located in the state of Pará, corresponds to the region near to Altamira city. Both study area locations are shown in Fig. 1(a).

ALOS PALSAR L-band polarimetric images were considered in the experiments. While an image acquired on April 23, 2007 was adopted for the first area (the Tapajós National Forest region), the second study area (the Altamira region) is represented by an image acquired on March 20, 2009.

According to reports from the Brazilian National Institute of Meteorology [32], April 2007 and March 2009 were both rainy periods in the Tapajós National Forest and Altamira areas. Although rain exerts an influence on target backscatter, and consequently, may impair the separability between such targets, it is important/reasonable to carry out the analysis in weather conditions where radar data has practical application advantages compared to optical data.

Geometrical correction procedures were carried out on these images. The first step performed was the conversion from slant to ground range geometry followed by a 3×3 multilook processing. The resulting images from these processes were georeferenced based on data provided by the U.S. Geological Service [33]. It is worth mentioning that when the slant-to-ground range conversion was performed, a supersampling was considered to agree the pixel spacing in both ground and azimuth directions in approximately 3.6 m. The resulting images after the multilook processing presented a pixel spacing with approximately 10 m. Furthermore, the nearest neighbor resampling method was adopted in the slant-to-ground range conversion as in the geo-referencing steps in order to preserve the statistical proprieties of the data. No filtering process for speckle reduction was carried out to preserve the statistical proprieties of the data. Finally, a clipping process delimited the Tapajós and Altamira images in 1500×3000 and 2900×1900 pixels wide, respectively.

Eleven land cover classes were identified in the Tapajós National Forest area: primary forest (PF), degraded forest (DF), old regeneration stage (OR), intermediate regeneration stage (IR), new regeneration stage (NR), clean pasture (CP), dirty pasture (DP), and four types of agriculture (A1, A2, A3, and A4). This area is very well known and has been the object of studies since the 70s. Identification of the aforementioned classes was based on field information collected in 2005 and 2007 reports of local researchers, especially for crops identification, and on temporal analysis of LANDSAT-5 TM images gathered over the period from 1984 to 2007. Similarly, with a basis in field information,

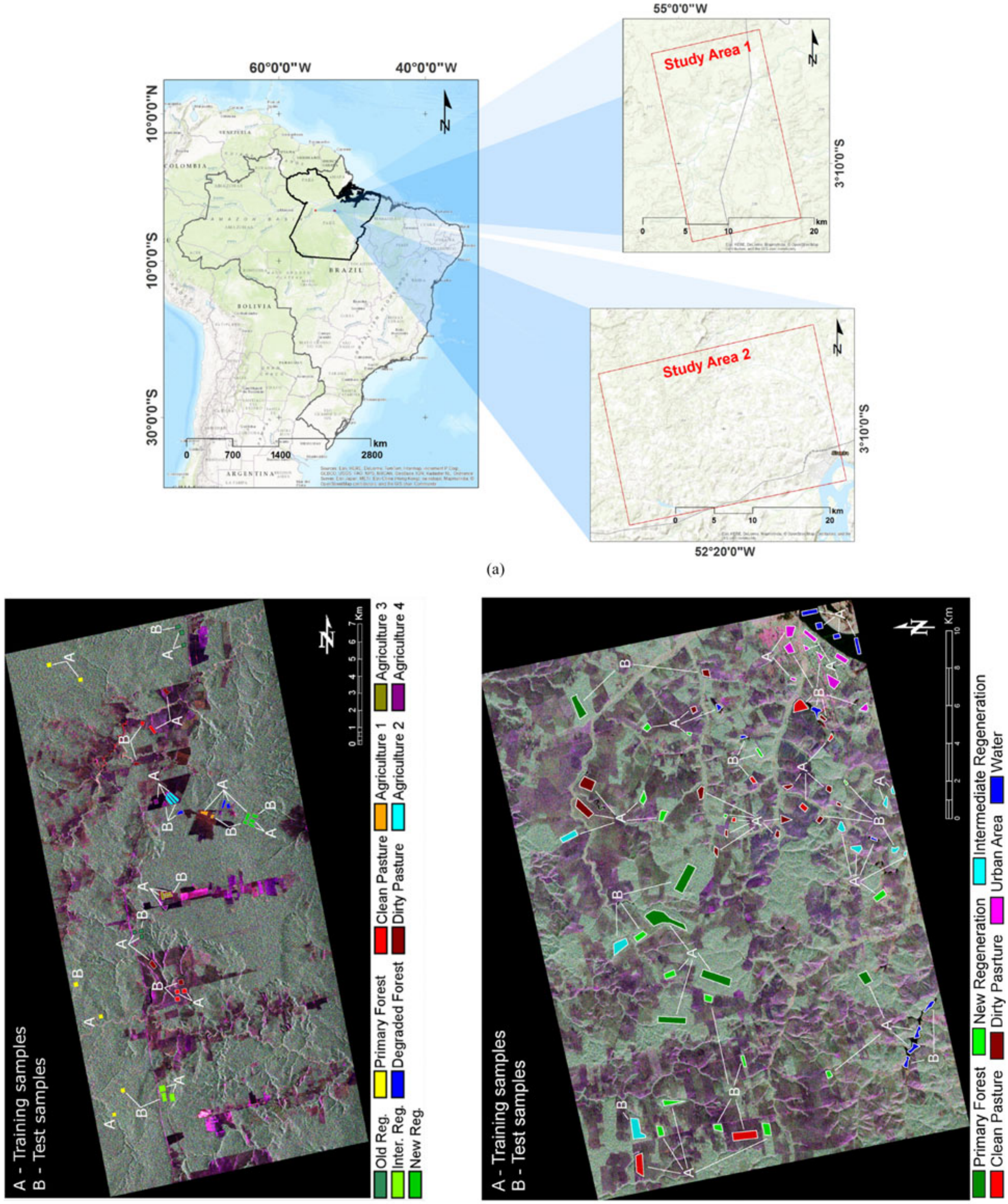

Fig. 1. Study areas, images, and selected samples. (a) Study area location. (b) ALOS PALSAR data and selected samples for the Tapajós National Forest region (study area 1). (c) ALOS PALSAR data and selected samples for the Altamira region (study area 2).

temporal analysis of LANDSAT-5 TM images, and considering the land use/cover characterization provided by the TerraClass project [34], the classes PF, IR, NR, CP, DP, urban area (UA), and water (WA) were identified in the Altamira area.

PF presents four layers with approximately 360 trees/ha. Dominant trees present diameter at breast height (DBH) mean values of 42 cm and a height above 25 m; aboveground biomass is typically 220 tons/ha. The old, intermediate, and new regeneration stages selected correspond to areas with more than 20 years, 10–20 years, and less than 10 years of having undergone regeneration, respectively. Old regeneration can reach up to 150 tons/ha, and DBH between 11 and 18 cm. IR has an

TABLE I
QUANTITY OF PIXELS FOR THE TRAINING SAMPLES AND TEST SAMPLES OF EACH LAND COVER CLASS IN THE TAPAJÓS AREA

Class	Training		Testing	
	Pixels	Polygons	Pixels	Polygons
PF	1 967	4	1 083	2
DF	1 171	2	587	1
OR	1 920	4	989	2
IR	2 235	2	1 013	1
NR	1 834	3	954	2
CP	1 799	3	1000	2
DP	1 825	2	1 237	2
A1	590	1	259	1
A2	1 660	2	799	1
A3	977	2	496	1
A4	906	2	490	1
Total	16 884	27	8 907	16

TABLE II
QUANTITY OF PIXELS FOR THE TRAINING SAMPLES AND TEST SAMPLES OF EACH LAND COVER CLASS IN THE ALTAMIRA AREA

Class	Training		Testing	
	Pixels	Polygons	Pixels	Polygons
PF	23 188	6	11 911	2
IR	14 084	11	6 220	6
NR	10 405	6	5 046	3
CP	5 654	4	9 115	3
DP	14 998	10	2 898	4
UA	8 198	6	3 149	3
WA	8 071	8	3 651	4
Total	84 598	51	41 990	25

average height of about 8 m, a DBH around 8 cm, and an aerial biomass of about 28 tons/ha; NR has an average height around 6 m, a DBH of 6 cm, and a biomass of 10 tons/ha.

Degraded forest refers to primary forest areas that were partially cut down. The basic difference between clean and dirty pasture is the vegetative cover density: Clean pasture shows lower density vegetation, mostly grass, than dirty pasture, which is covered with sparse shrubs. Over time, pasture areas generally had their vegetation removed for the development of economic activities. The agricultural types identified were related to different growing stages and culture species.

Fig. 1 shows the study areas and the land cover samples considered for each area. It is important to mention that the land cover samples identified in the study area were initially randomly divided into two main sets designated for training the methods and testing the classification results, as indicated in Fig. 1(b) and (c) by "A" and "B." The training set was intentionally defined with approximately double the number of polygons in each class compared to the test set. To remove spatial correlation between the pixels inside the training and test polygons, a resampling was performed considering a regular grid with a lag of three pixels in both the vertical and horizontal directions. Tables I and II present the number of pixels and polygons of the training and test samples for each study area.

To provide a systematic assessment, a configuration of several sets with different amounts of classes, called scenarios, were constructed. These scenarios were built to try to merge classes that are closest to each other, in the attribute space, as determined by a methodology proposed in Section III-B. Training and test data are also merged when two classes are merged.

B. Scenarios Definition

In order to support the analysis about the capability of fully polarimetric data for discrimination of thematic classes in rain forest areas, a methodology for the definition of thematic classes, and its hierarchical organization in scenarios, from an initial set of primary classes is proposed. Scenarios are understood as any set of thematic classes that defines a classification problem. When considering different scenarios, it is possible to assess the discriminative capability of different thematic classes as well as the overall performance provided by a particular image, for instance, full polarimetric and its polarization subsets and/or a classification method.

The scenarios decomposition scheme is based on the single-link hierarchical clustering (SLHC) algorithm [29]. As an overview about this algorithm, from a set of *elements* and a fixed threshold, the central concept of SLHC consists of defining groups in which, for each element of the group, there is at least one other element in the same group with *dissimilarity* inferior to the threshold.

For the purposes of this study, considering that the *elements* are probability density functions, that represent the different thematic classes previously modeled with basis on *a priori* information (i.e., samples), and that the *dissimilarity* between these elements is obtained by adopting a stochastic distance between such probability density functions, it is possible to apply the SLHC algorithm to define groups of thematic land cover (or thematic) classes. The application of SLHC considering different thresholds produces a hierarchical organization over the land cover classes. The groups defined depend on the thresholds adopted and define the *scenario classes*.

Formally, let $\Omega = \{\omega_1, \omega_2, \ldots, \omega_c\}$ be an initial set of classes, $d(\omega_i, \omega_j)$, the stochastic distance between probability distributions modeled for the elements of the classes ω_i and ω_j and S_φ a partition set of Ω with cardinality φ formed by elements, or the *scenario classes*, $\varpi_{p\varphi}$, $p = 1, \ldots, \varphi$. Under these conditions, for a defined threshold $T \in \mathbb{R}_+$, a unique partition, or scenario, $S_\varphi^T = \left\{\varpi_{p\varphi}^T : p = 1, \ldots, \varphi\right\}$ is defined, which satisfies the following conditions:

1) $\forall i \neq j; d(\omega_i, \omega_j) > T \Leftrightarrow \omega_i \in \varpi_{p\varphi}^T; \#\varpi_{p\varphi}^T = 1;$
2) $\exists i \neq j; d(\omega_i, \omega_j) < T \Leftrightarrow \omega_i \in \varpi_{p\varphi}^T; \omega_j \in \varpi_{q\varphi}^T; p \neq q;$
3) $\exists i \neq j; d(\omega_i, \omega_j) \leq T \Leftrightarrow \omega_i \in \varpi_{p\varphi}^T; \omega_j \in \varpi_{p\varphi}^T;$
4) $\forall i \neq j; \omega_i \in \varpi_{p\varphi}^L; \omega_j \in \varpi_{q\varphi}^L; d(\omega_i, \omega_j) \leq M$
$L \leq M \Rightarrow \varpi_{p\varphi}^L \bigcup \varpi_{q\varphi}^L \subseteq \varpi_{r\varphi'}^M; \varphi' < \varphi.$

Condition (1) allows for the definition of the scenario classes formed from a single class of Ω, whereas (2) indicates that two classes of Ω must be incorporated into different scenarios when the stochastic distance between the probabilistic distributions is greater than the fixed threshold T. However, when the distance between the classes of Ω is less than or equal to T, the classes

$d(\omega_i,\omega_j)$	ω_1	ω_2	ω_3	ω_4
ω_1	0	l_1	l_4	l_3
ω_2	l_1	0	l_5	l_6
ω_3	l_4	l_5	0	l_2
ω_4	l_3	l_6	l_2	0

Where:
$0{=}T_0 \leqslant l_1 < T_1 \leqslant l_2 < T_2 \leqslant l_3 < T_3 \leqslant l_4 < l_5 < l_6$
and the matrix above represents dissimilarity measures $d(\omega_i,\omega_j)$ between each class.

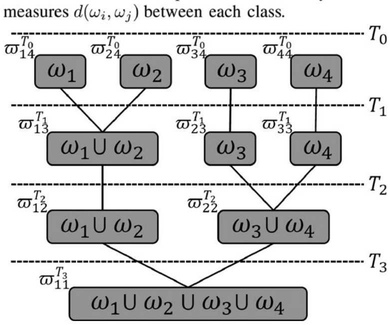

Fig. 2. Example of scenario definition. Table of measured distances between classes (top) and scenario definition based on the proposed methodology (bottom).

must be incorporated into the same scenario, as expressed by condition (3). The last condition is related to the central concept of the SLHC algorithm.

Fig. 2 presents an example in which scenarios from an initial set of four classes are defined. Initially, by adopting a threshold T_0, scenarios composed of a single primary class of Ω are defined. When a threshold T_1 is adopted, and it is known that the distance between ω_1 and ω_2 is less than T_1 (i.e., $d(\omega_1,\omega_2) \leq T_1$), a new scenario class is generated, which is represented by $\varpi_{13}^{T_1}$ [condition (3)]. However, for classes ω_3 and ω_4, whose interclass distance is, like that between ω_1 and ω_2, greater than T_1, no union occurs [condition (2)], but for a new threshold $T_2 > T_1$, the classes ω_3 and ω_4 are merged ($d(\omega_3,\omega_4) \leq T_4$) [condition (3)]. Finally, for a threshold T_3, it is possible to affirm that there is at least one element $\omega_i \in \varpi_{12}^{T_3}$ and at least one element $\omega_j \in \varpi_{22}^{T_3}$, between which the distance is less than T_3 (i.e., $d(\omega_1,\omega_4) = l_3 \leq T_3$ [(condition (4)], thus ending the scenario definition process.

A convenient way to define the thresholds is by computing the dissimilarity values (via stochastic distance) between each possible pair of initial classes and sorting these values in ascending order. Ranging from the smaller to the higher dissimilarity value, threshold values will be found that meet the condition (3), and consequently, define new scenarios.

C. General Experiment Design

Fig. 3 depicts the experiment design of this research. The same procedures are applied in both study areas (i.e., the Tapajós National Forest and Altamira).

Initially, considering the full polarimetric image and the respective set of primary land cover classes, the scenario decomposition (see Section III-B) is performed (phase A). It is worth noting that as more primary classes are in the Tapajós National Forest area, more scenarios are defined to this area in comparison to Altamira.

Concomitantly, all possible subsets of polarization combinations are generated from the fully polarimetric data (phase B). Such combinations produce single-, dual-, and multipolarized images. Single-polarized images are denoted by HH, HV, and VV; dual-polarized images by HH+HV, HH+VV, and HV+VV; and multipolarized images by HH+HV+VV. The fully polarimetric image will be denoted by FP when convenient. The mentioned polarization combinations are considered in the analysis in order to verify if fully polarimetric data, as a baseline, provides a significantly better capability to deal with different classification scenarios in tropical regions compared to subsets of polarization with just amplitude/intensity information.

It is important to stress that the definition of the scenarios (phase A) is performed using only fully polarimetric data. This procedure defines different class configurations (scenarios) that can be considered in the classification process independent of whether the adopted image is single-, dual- or multipolarized, or fully polarimetric.

After the definition of the scenarios, the datasets are defined to train the classification methods analyzed in this study and to test the respective results in each scenario (phase C). It is worth note that the primary land cover samples are organized into "training and test samples," as shown in Fig. 1(b) and (c). When two primary classes are merged (in phase A), samples of such classes initially designated for training are merged into a new class, and these samples, which represent this newer class, remains for training. The same consideration is made for test samples.

Given the full polarimetric data and all polarization combinations (in phase B) as the training and test sample sets for each scenario (in phase C), the MLC training is carried through the parameter estimation of a probability density function for each class in each scenario (phase D). Adherence tests are carried out for each class when single-polarized (Square Root of Gamma, $K_{\text{Amplitude}}$ and $G^0_{\text{Amplitude}}$) and fully polarimetric (Wishart, K_{Complex}, and G^0_{Complex}) images are adopted (see Section II-A). Similarly, tuning the parameters via a grid search procedure, the SVM training is performed for each dataset, except for fully polarimetric data (phase E).

After the training process, pixel-wise classifications are produced by the MLC and SVM for each dataset and scenario (phase F). Contextual classifications are obtained by applying the ICM algorithm on the MLC and SVM results (phase G). Finally, the contextual classification results are assessed using the kappa coefficient of agreement and performing hypothesis tests to check the statistical significance between such results (phase H).

D. Results and Discussions

Considering the initial set of primary classes identified and the methodology proposed in Section III-B, eight and five scenarios were defined for the Tapajós and Altamira study areas, respectively.

The Bhattacharyya, Kullback–Leiber, and Hellinger stochastic distances between complex Wishart distributions [35] computed from the fully polarimetric information from the training samples were considered to measure the dissimilarity between the classes. For each study area, identical scenarios were defined

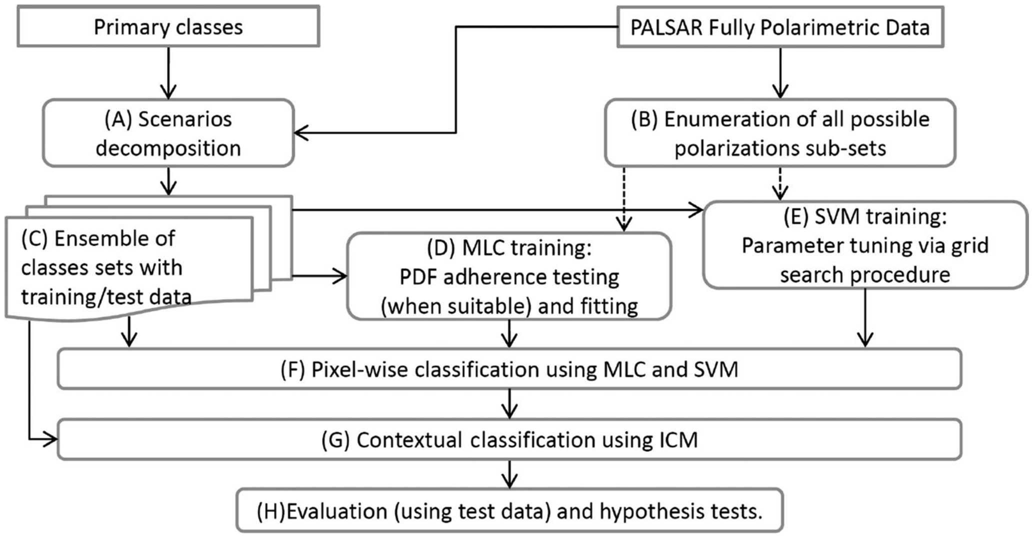

Fig. 3. General flowchart methodology.

TABLE III
ORGANIZATION OBTAINED FOR THE HIERARCHICAL SCENARIOS FOR THE TAPAJÓS NATIONAL FOREST STUDY AREA

Scenario/# of Classes	Classes											Threshold $\times 10^{-3}$
1/11	PF	OR	IR	NR	DF	CP	DP	A1	A3	A2	A4	0.00
2/10	PF	OR+IR		NR	DF	CP	DP	A1	A3	A2	A4	3.93
3/9	PF	OR+IR+NR			DF	CP	DP	A1	A3	A2	A4	11.29
4/8	PF+OR+IR+NR				DF	CP	DP	A1	A3	A2	A4	19.16
5/7	PF+DF+OR+IR+NR					CP	DP	A1	A3	A2	A4	25.37
6/6	PF+DF+OR+IR+NR					CP	DP	A1+A3		A2	A4	44.83
7/5	PF+DF+OR+IR+NR					CP+DP		A1+A3		A2	A4	152.86
8/4	PF+DF+OR+IR+NR					CP+DP+A1+A3				A2	A4	190.69

TABLE IV
ORGANIZATION OBTAINED FOR THE HIERARCHICAL SCENARIOS FOR THE ALTAMIRA STUDY AREA

Scenario/# of Classes	Classes							Threshold $\times 10^{-2}$
1/7	PF	IR	NR	CP	DP	UA	WA	0.00
2/6	PF	IR+NR		CP	DP	UA	WA	1.02
3/5	PF+IR+NR			CP	DP	UA	WA	1.08
4/4	PF+IR+NR			CP+DP		UA	WA	6.55
5/3	PF+IR+NR+CP+DP					UA	WA	12.18

independently of the adopted stochastic distance. Faced with this equivalence of the stochastic distances, the Bhattacharyya distance was adopted in this study.

Table III presents the scenarios obtained and their respective thresholds that define the classes of these scenarios for the Tapajós National Forest area. In this table, the symbol "+" represents the merging of classes. Similarly, Table IV presents the scenarios and respective thresholds for the Altamira study area. The different threshold values were obtained following the procedure described at end of Section III-B.

Each scenario defined for its corresponding study area was classified by the MLC/ICM method using fully polarimetric and single-, dual-, and multipolarized images. The SVM/ICM was also adopted to classify each defined scenario, but just for real spaces, that is, single-, dual-, and multipolarized images.

As previously discussed in Section III-C, when classifications using single-polarized and full polarimetric images are performed through the MLC method, a statistical distribution is selected from among those mentioned in Section II-A (square root of gamma, $K_{\text{Amplitude}}$, $G^0_{\text{Amplitude}}$, Wishart, K_{Complex}, and G^0_{Complex}) for each class in each scenario, based on which distribution best fitted the behavior of the class. A χ^2 test was carried out in order to verify the adherence of the training samples of each class to the distributions considered, thus indicating the best fitting distribution. For dual- and multipolarized images, the distribution presented in [36] and the multivariate Gaussian distribution were adopted, respectively.

The SVM method was used considering the OAA multiclass strategy. Preliminary tests indicated that the polynomial kernel function was the most suitable for the study

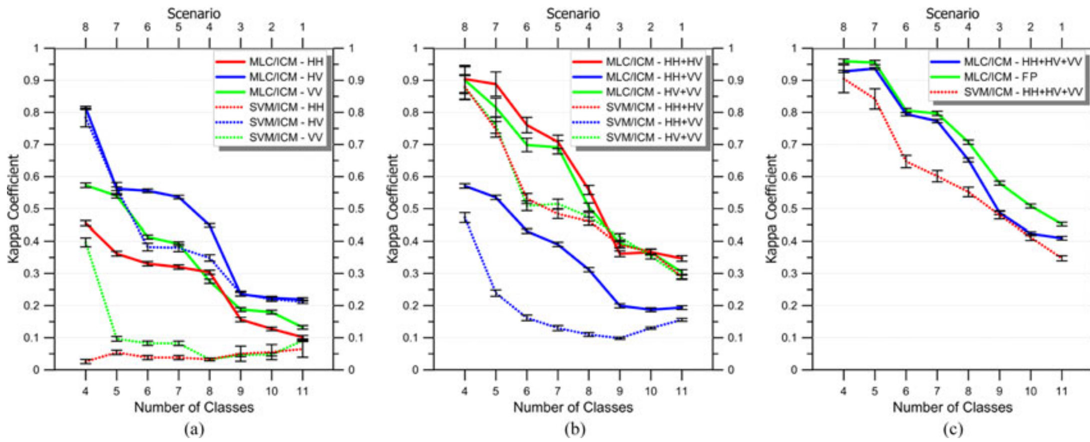

Fig. 4. Graphical comparison of the *Kappa* coefficients obtained with single-, dual-, and multipolarized and fully polarimetric data for the Tapajós National Forest study area. Error bars represent one standard deviation. (a) Single-polarized data. (b) Dual-polarized data. (c) Multi-polarized and fully polarimetric data.

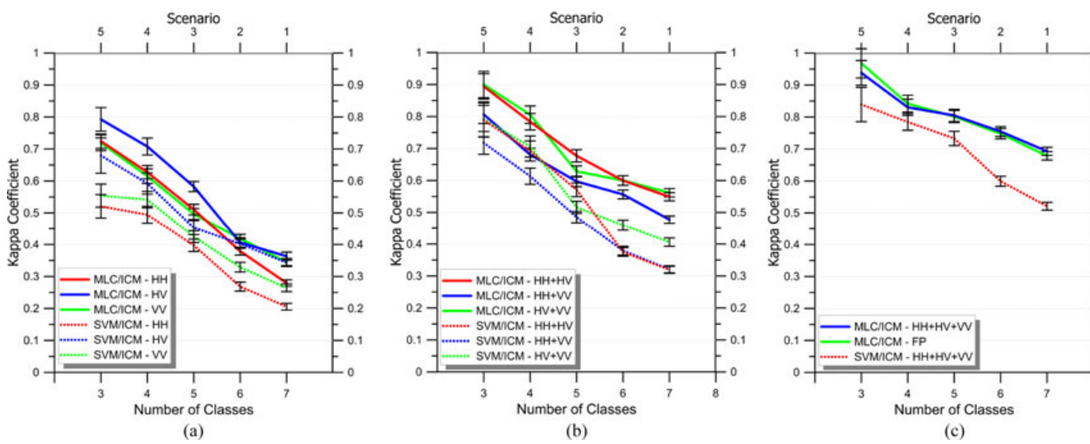

Fig. 5. Comparison of the kappa coefficients obtained with single-, dual-, and multipolarized and fully polarimetric data for Altamira study area. Error bars represent one standard deviation. (a) Single-polarized data. (b) Dual-polarized data. (c) Multi-polarized and full polarimetric data.

TABLE V

BEST RESULTS FOR EACH SCENARIO FOR THE TAPAJÓS NATIONAL FOREST STUDY AREA MULTIPLE ENTRIES IN EACH FRAME ARE STATICALLY EQUAL AT 90%

Scenario	Classes	Single Polarized	Dual Polarized	Multipolarized and Fully Polarimetric	Best Classification (*Kappa*)
1	11	M-HV, S-HV	M-HH+HV	M-FP	M-FP (0.4521)
2	10	M-HV, S-HV	M-HH+HV, M-HV+VV S-HH+HV, S-HH+VV	M-FP	M-FP (0.5884)
3	9	M-HV, S-HV	M-HH+HV, S-HH+HV	M-FP	M-FP (0.5796)
4	8	M-HV	M-HH+HV	M-FP	M-FP (0.7072)
5	7	M-HV	M-HH+HV, M-HV+VV	M-FP	M-FP (0.7969)
6	6	M-HV	M-HH+HV	M-HH+HV+VV, M-FP	M-HH+HV+VV (0.7947)
7	5	M-HV, S-HV	M-HH+HV	M-FP	M-FP (0.9553)
8	4	M-HV, S-HV	M-HH+HV, M-HV+VV S-HH+HV, S-HH+VV	M-FP	M-HH+HV (0.9041)

[1]M stands for MLC and S stands for SVM classifier.

data obtained, rather than the radial basis and function. The selection of adequate C (penalty) and q (degree of polynomial kernel) parameters, admitting the search space $C \in \{0.1, 1, 10, 100, 1000, 10000\}$ and $q \in \{1, 2, 3, 4, 5\}$, was based on a grid search process with tenfold cross validation, as discussed in [37].

The cross-validation folders are built in consideration of the training sample set corresponding to the analyzed scenario. For each folder, this initial training sample set is randomly split into two subsets, to train the SVM and to validate such training given a parameter configuration. The size of the training subset corresponds to 67% of the pixels of each class from the initial

TABLE VI
BEST RESULTS FOR EACH SCENARIO FOR THE ALTAMIRA STUDY AREA MULTIPLE ENTRIES IN EACH FRAME ARE STATICALLY EQUAL AT 90%

Scenario	Classes	Single Polarized	Dual Polarized	Multipolarized and Fully Polarimetric	Best Classification (*Kappa*)
1	7	M-HV	M-HH+HV, M-HV+VV	M-HH+HV+VV, M-FP	M-HH+HV+VV (0.6929)
2	6	M-HV	M-HH+HV, M-HV+VV	M-HH+HV+VV, M-FP	M-HH+HV+VV (0.7545)
3	5	M-HV, M-VV	M-HH+HV	M-HH+HV+VV, M-FP	M-HH+HV+VV (0.8487)
4	4	M-HV	M-HH+HV, M-HV+VV	M-HH+HV+VV, M-FP	M-HH+HV+VV (0.8303)
5	3	M-HV	M-HH+HV, M-HV+VV S-HV+VV	M-HH+HV+VV, M-FP	M-HH+HV+VV (0.9379)

[1]M stands for MLC and S stands for SVM classifier.

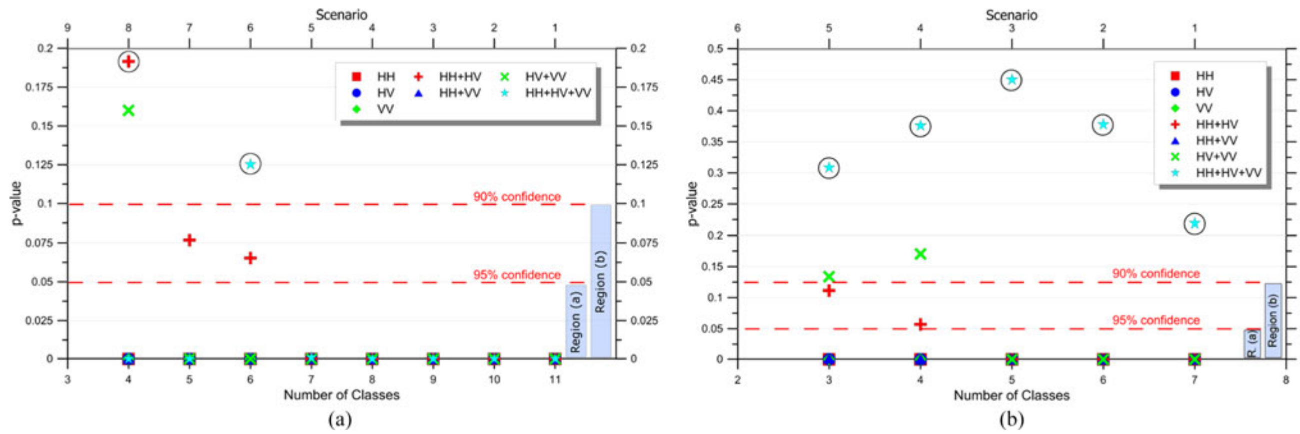

Fig. 6. p-values from a hypothesis test comparing the kappa coefficient values from fully polarimetric results, adopted as a baseline (not shown), with single-, dual-, and multipolarized results obtained by the MLC/ICM method. The circled results mean that the Kappa coefficient values of the results using fully polarimetric images was not the best in this case. The results in region (a) mean that the best kappa coefficient was significantly better than the appointed one at a 95% confidence level, while results in region (b) mean that the appointed values were better than the best one only at 90% confidence level.

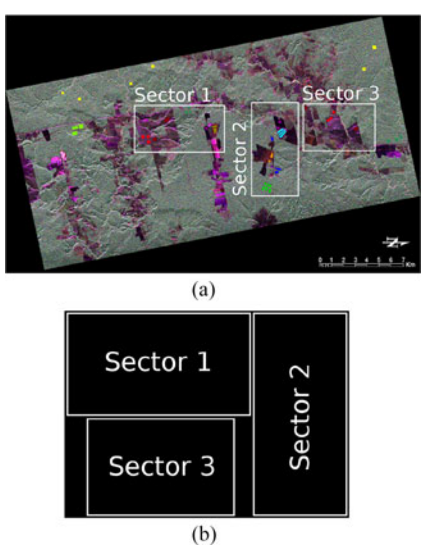

Fig. 7. Selected sectors used to show the classification results for the Tapajós National Forest area. (a) Regional sectors. (b) Sector arrangement.

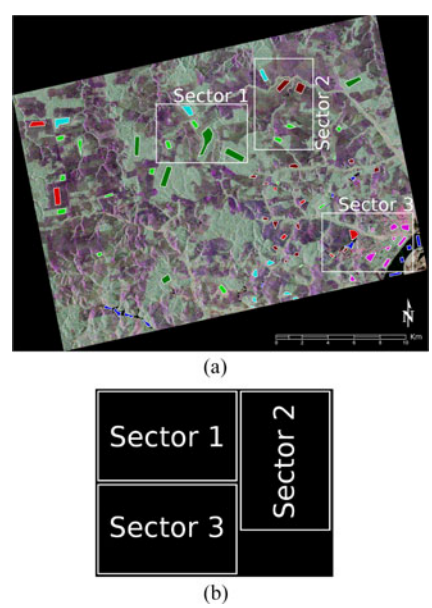

Fig. 8. Selected sectors used to show the classification results for the Altamira study area. (a) Regional sectors. (b) Sector arrangement.

training sample set. The validation subset is complementary to the training subset with respect to the initial training sample set. It is worth mentioning that the cross-validation folders are initially fixed, and then, each parameter configuration is assessed in consideration of such folders.

With respect to the ICM algorithm, in addition to the MLC and SVM, a minimum change of 5% between two iterations or a maximum of eight iterations was applied as a convergence criterion. The neighborhood, defined by $\mathcal{V}(i)$ in (11), corresponded to a spatial-geographic window of 3×3 pixels wide, and the pseudo likelihood function [38] was adopted to tune the β parameter in (11).

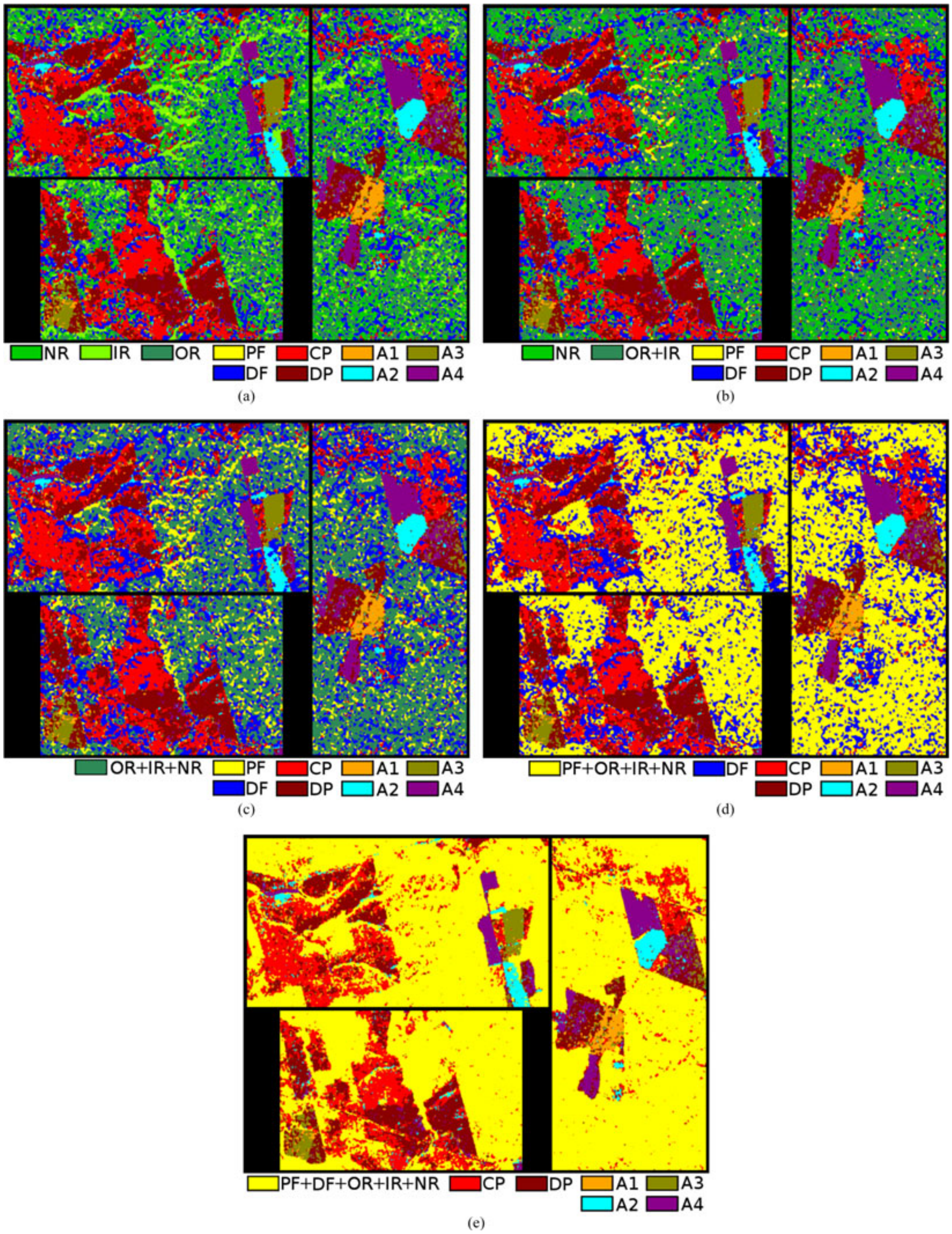

Fig. 9. Classification results obtained for scenarios 1–5 using full polarimetric data in the Tapajós National Forest area. (a) Scenario 1: MLC/ICM - FP. (b) Scenario 2: MLC/ICM - FP. (c) Scenario 3: MLC/ICM - FP. (d) Scenario 4: MLC/ICM - FP. (e) Scenario 5: MLC/ICM - FP.

Considering the single-, dual-, and multipolarized and fully polarimetric[4] images from Tapajós National Forest, the respective eight scenarios defined, and the MLC/ICM and SVM/ICM methods, a total of 120 classification results were obtained.[5] Analogously, through the single-, dual-, and multipolarized and fully polarimetric images from the Altamira area, the same classification methods, and the five scenarios, 75 classification results were obtained.[6]

[4]It must be stressed that this image was only classified by the MLC/ICM method.

[5]Excluding the polarimetric data, there are seven datasets (HH, HV, VV, HH+HV, HH+VV, HV+VV, and HH+HV+VV), eight scenarios, and two classifiers, producing $7 \times 8 \times 2 = 112$ classification results. Since only MLC/ICM was applied to the fully polarimetric data, eight more classifications were obtained, giving a total of 120 classifications.

[6]It is, considering the seven polarized datasets, five scenarios and two classifiers (MLC/ICM and SVM/ICM) and the additionalfive scenarios processed by MLC/ICM on fully polarimetric data, we have a total of 75 classification results.

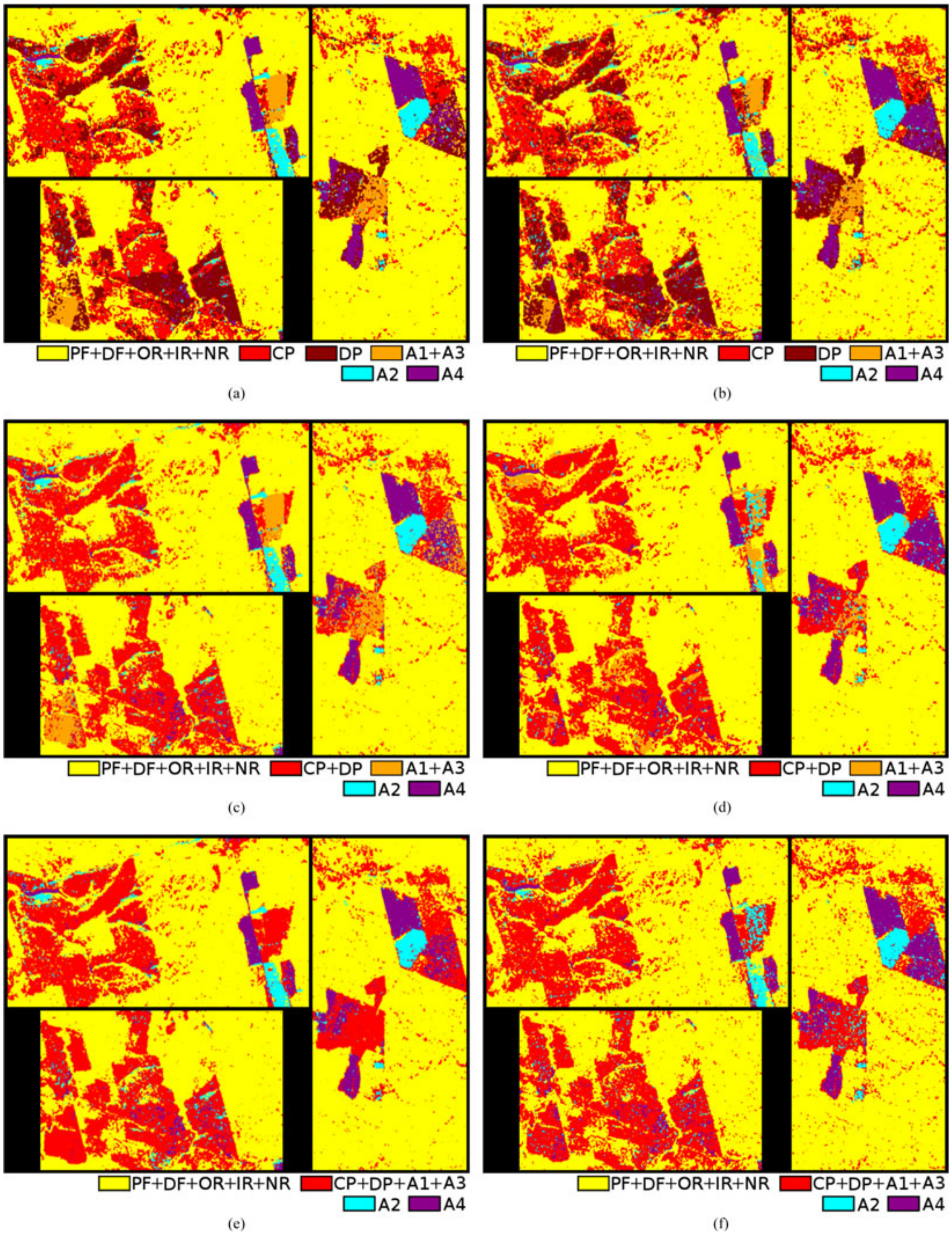

Fig. 10. Comparison of the classification results obtained for scenarios 6–8 using full polarimetric and polarized data in the Tapajós National Forest area. (a) Scenario 6: MLC/ICM - FP. (b) Scenario 6: MLC/ICM - HH+HV+VV. (c) Scenario 7: MLC/ICM - FP. (d) Scenario 7: MLC/ICM - HH+HV. (e) Scenario 8: MLC/ICM - FP. (f) Scenario 8: MLC/ICM - HH+HV.

The kappa coefficient values for each classification result of the Tapajós and Altamira study areas are presented in Fig. 4(a)–(c) and Fig. 5(a)–(c), respectively. For convenience, the results obtained from single-, dual-, and multipolarized images are presented separately. The results obtained from fully polarimetric images are presented together with those obtained for the multipolarized ones.

Based on a bilateral 90% confidence hypothesis test to compare the kappa coefficients [31], Tables V and VI identify the statistically most accurate results obtained using a specific method and image for the Tapajós and Altamira areas. If two methods were statistically indifferent, both were denoted in these tables. The best result found for each scenario was also indicated in Tables V and VI. In the case of results that were statistically indifferent and considered the best, the result with the smaller number of polarizations was considered to be better. To simplify the notation system, MLC/ICM and SVM/ICM were denoted by M and S, respectively.

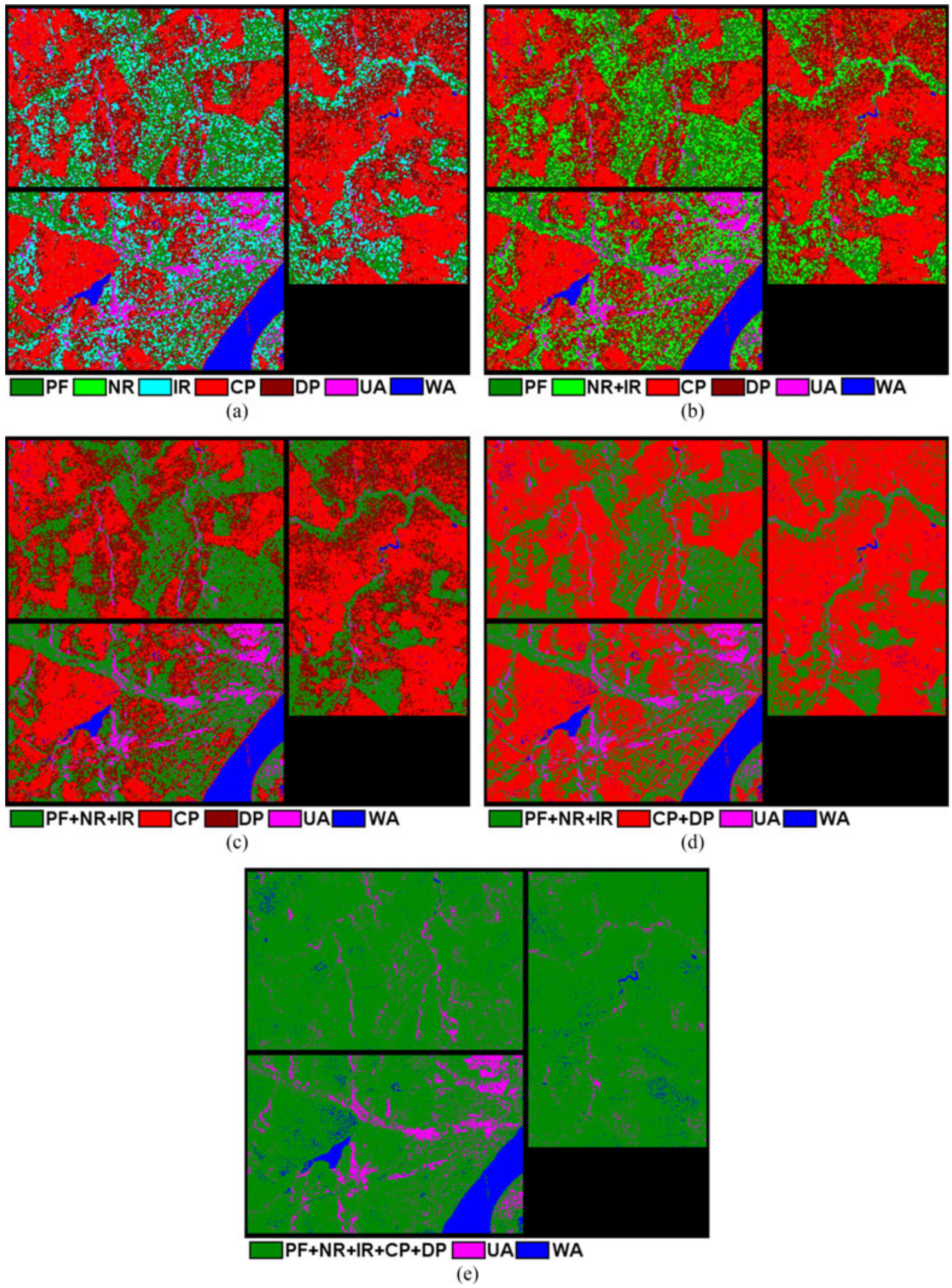

Fig. 11. Classification results obtained for scenarios 1–5 using multipolarized data in the Altamira area. (a) Scenario 1: MLC/ICM - HH+HV+VV. (b) Scenario 2: MLC/ICM - HH+HV+VV. (c) Scenario 3: MLC/ICM - HH+HV+VV. (d) Scenario 4: MLC/ICM - HH+HV+VV. (e) Scenario 5: MLC/ICM - HH+HV+VV.

From both Tables V and VI, it is possible to note the importance of HV polarization for discriminating purposes considering all scenarios.

Considering an *ad hoc* minimum quality as a kappa value equal to 0.8, it is possible to suggest that L-band data allows for discriminate pasture types and some agricultural varieties when using fully polarimetric or multipolarized data. On the other hand, no discrimination between any high biomass targets (i.e., forest and regeneration types) was identified.

Figs. 4(a) and 5(a) show the kappa coefficient values of the classification results obtained with single-polarized images in the Tapajós and Altamira areas. These results reveal that in most of the scenarios, the most accurate coefficients were associated with classifications obtained when the HV image was used. Furthermore, it is possible to observe that by using the HV image, MLC/ICM produces results that are equivalent or superior to those produced by SVM/ICM in both study areas. Additionally, SVM/ICM showed less accuracy when using HH and VV images.

Regarding the classifications obtained using dual-polarized images, it can be noted that HH+HV and HV+VV produced similar results. In addition, the MLC/ICM method yielded greater or similar accuracy as compared to the SVM/ICM method. These observations may be verified in Figs. 4(b) and 5(b).

According to the behavior illustrated in Fig. 4(c) about classification results in the Tapajós area, when MLC/ICM is adopted, the kappa coefficients obtained with the fully polarimetric image are superior to those obtained using the multipolarized image, except for scenario 6, in which the two classifications are statistically equal. Regarding the Altamira area, multipolarized and fully polarimetric images provide statistically equal results in all scenarios, as shown in Fig. 5(c) and Table IV. The SVM/ICM exhibits inferior performance in most of the scenarios observed in both study areas.

A general trend characterized by low kappa coefficients may be observed in the first scenarios in both study areas, independent of the images and classification methods used. This behavior is justified by the existence of classes with low separation ability (low contrast). The claim regarding low separation ability between classes is manifested in the threshold values adopted in defining the scenarios, as shown in Tables III and IV. As the number of classes, and consequently, the complexity of the scenarios, decreases, there is a gradual increase in accuracy.

The SVM/ICM method tends to produce less accurate results, or similar results in some cases, as compared to those obtained by MLC/ICM. Thus, based on these case studies, it appears that the MLC/ICM method is more suitable than the SVM/ICM one for the classification of land cover types in a study area using L-band SAR images. The use of proper statistical distributions for SAR data by the MLC/ICM method is a factor that justifies its superiority in comparison to the SVM/ICM in this study.

Illustrative comparisons in Fig. 6 show p-values from hypothesis tests (kappa equality) that compare the classification results obtained using fully polarimetric images to the polarized images for the Tapajós and Altamira study areas, respectively. Since the best classifications were achieved using the MLC/ICM method, the SVM/ICM method was not included in these analyses. Datasets above the 90% dashed line may be considered statistically equivalent, with 90% confidence. The 95% dashed lines were included to show that almost all the results were still different from those with fully polarimetric images.

As can be seen, with respect to the Tapajós study area [see Fig. 6(a)], fully polarimetric images definitely provided the better results for scenarios 1–5 (although with poor Kappa coefficient values), but for scenarios 6 and 8, some alternative datasets were equivalent at 90%. Although fully polarimetric was superior for scenario 7, HH+HV was close to being statistically equal at 90% confidence and may be considered equal at 95%. Observing the results for the Altamira area [see Fig. 6(b)], it can be verified that equivalent results are provided with nonfully polarimetric images, in most of the cases by the multipolarized data, independently of scenario. Especially for scenarios 4 and 5, statistically indifferent results with 95% and 90% confidence levels were obtained when HH+HV and HV+VV dual-polarized images are compared to full polarimetric, respectively. Furthermore, these graphs reinforce again the importance of HV polarization since all the datasets similar to fully polarimetric sets have this polarization as a component.

After carrying out the aforementioned quantitative evaluations, Figs. 9–11 show relevant classification results for the Tapajós and Altamira regions. Due to the size of the images, just three sectors from each study areas are shown. These sectors are represented in Figs. 7(a) and 8(a) and sector arrangements, adopted as the reference in Figs. 9–11, are defined in Figs. 7(b) and 8(b), respectively.

Fig. 9 shows the classifications for scenarios 1–5, where the fully polarimetric image was superior to any of the other datasets. The difficulty involved in adequately separating the regeneration, primary forest and degraded forest classes is clearly apparent. A more consistent classification was obtained when these classes were merged into a single class (scenario 5). On the other hand, the pastures and agricultural classes were adequately classified.

The classifications of scenarios 6–8 are presented in Fig. 10. Specifically, Fig. 10(a) and (b) compare the full polarimetric and HH+HV+VV images, respectively, in scenario 6; Fig. 10(c)–(f) compare the fully polarimetric and HH+HV in scenarios 7 and 8. The most perceptive differences were found when the forest class (i.e., PF+DF+OR+IR+NR) was observed. Classifications using full polarimetric data tend to be less noisy than those using polarized data. Agricultural classes are also better classified with the full polarimetric data.

These figures confirm that the standard availability of HH+HV of PALSAR data was a sensible choice, where considering an adequate classification method, this dual-polarized dataset can provide results similar to those obtained when using the fully polarimetric dataset. The classification of results obtained in the Altamira area, as illustrated in Fig. 11, confirm the discussions previously presented for the Tapajós study area. Initially, it can be observed in scenarios 1 and 2 [see Fig. 11(a) and (b)] the low discriminability between primary forest and regeneration areas. The union of these types of targets into a single class produces more consistent results [see Fig. 11(c)]. However, urban areas are commonly misclassified as high biomass targets (i.e., forest or regeneration types), as shown in Fig. 11(d). As observed in the results for the Tapajós area, clean and dirty pasture areas may be distinguishable using multipolarized data. Water, usually considered a trivial classification target, was adequately identified in all scenarios.

IV. Conclusion

The objective of this study was to carry out an assessment of the use of L-band fully polarimetric images for mapping land cover classes in Amazon regions. For this purpose, the use of fully polarimetric images (considered as baseline data) were compared to all possible subsets of polarizations in amplitude/intensity. The MLC, considering appropriate distributions for SAR data, and SVM methods were adopted to perform the classification of such images. The ICM algorithm was used to include the contextual information on the MLC and SVM results, and then, improve the classification accuracies.

To support the aforementioned analysis, a methodology for defining scenarios was proposed. The scenarios defined through this methodology state an organization of different thematic classes with a hierarchical relationship. In general, starting from a sample set of primary classes observed on fully polarimetric images, the scenarios and respective thematic classes are established with a basis on the concepts of the SLHC algorithm and stochastic distances. The classification of these scenarios and its simultaneous analysis allow assessing the capability offered by different image types (i.e., fully polarimetric or its subsets of polarizations) to discriminate distinct thematic classes.

Initially, a satisfactory separability of forest subtypes and regeneration stages with the use of fully polarimetric images or any other subset of polarizations [see Figs. 9(a)–(d) and 11(a)–(c)] was not verified.

However, studies that do not concern the classification of forest types and regeneration stages can be carried out, preferably using HH+HV+VV multipolarized images, as presented by Kappa values in Figs. 4(c) and 5(c) with respect to scenarios 5–8 (Tapajós area) and 3–5 (Altamira area), respectively. Furthermore, on the unavailability of multipolarized images, HH+HV or HV+VV dual-polarized images may produce satisfactory results, as illustrated in Figs. 4(b) and 5(b).

It is important to note that there is a tendency for the presence of HV polarization information to contribute to achieving higher accurate results. This conclusion is easily verified in the graphics of Figs. 4 and 5 (where higher kappa curves are assigned to datasets with HV) as by the hypothesis test performed to compare the accuracy of the results obtained with HH+HV and HV+VV images with that of the results obtained using full polarimetric data, as shown in Fig. 6(a) and (b).

It is noteworthy that for similar classification studies, as presented by scenario 8 in the Tapajós area, whose classes can be stratified into high, medium, low, and the absence of biomass, the use of HV single-polarized images tended to provide better results. Regarding the classification methods analyzed, it was concluded from this study that the use of the classification method MLC/ICM, based on statistical SAR modeling, was more appropriate than the use of the conventional SVM/ICM method.

Further studies, adopting the proposed methodology for the definition of scenarios but also considering other classification methods, textural features, and polarimetric attributes, for example, the well-known Freeman-Durden, Yamaguchi, and Cloude-Pottier features, should be carried out.

References

[1] D. Lu, Q. Chen, G. Wang, L. Liu, G. Li, and E. Moran, "A survey of remote sensing-based aboveground biomass estimation methods in forest ecosystems," *Int. J. Digit. Earth*, vol. 9, no. 1, pp. 1–43, 2014.

[2] R. N. Treuhaft *et al.*, "Biomass estimation in a tropical wet forest using Fourier transforms of profiles from lidar or interferometric SAR," *Geophys. Res. Lett.*, vol. 37, no. 23, 2010. [Online]. Available: http://dx.doi.org/10.1029/2010GL045608

[3] T. Neeff, G. S. Biging, L. V. Dutra, C. C. Freitas, and J. R. Santos, "Modeling spatial tree patterns in the Tapajós forest using interferometric height," *Rev. Bras. de Cartografia*, vol. 1, no. 57, pp. 1–6, 2005.

[4] W. Zhang, W. Wang, and L. Chen, "Constructing DEM based on InSAR and the relationship between InSAR DEM's precision and terrain factors," *Energy Procedia*, vol. 16, pp. 184–189, 2012.

[5] R. Lanari *et al.*, "Generation of digital elevation models by using SIR-C/X-SAR multifrequency two-pass interferometry: The Etna case study," *IEEE Trans. Geosci. Remote Sens.*, vol. 34, no. 5, pp. 1097–1114, Sep. 1996.

[6] S. Huang *et al.*, "A comparison of individual tree and forest plot height derived from lidar and InSAR," *Photogramm. Eng. Remote Sens.*, vol. 75, no. 2, pp. 159–167, 2009.

[7] T. Neeff, P. M. A. Graça, L. V. Dutra, and C. C. Freitas, "Carbon budget estimation in central Amazonia: Successional forest modeling from remote sensing data," *Remote Sens. Environ.*, vol. 94, no. 4, pp. 508–522, Feb. 2005.

[8] J. R. Santos, J. C. Mura, W. R. Paradella, L. V. Dutra, and F. G. Gonçalves, "Mapping recent deforestation in the Brazilian Amazon using simulated L-band MAPSAR images," *Int. J. Remote Sens.*, vol. 29, no. 16, pp. 4879–4884, 2008.

[9] C. F. Angelis, C. C. Freitas, D. M. Valeriano, and L. V. Dutra, "Multitemporal analysis of land use/land cover JERS-1 backscatter in the brazilian tropical rainforest," *Int. J. Remote Sens.*, vol. 23, no. 7, pp. 1231–1240, 2002.

[10] Z. Qi, A. G. Yeh, X. Li, and X. Zhang, "A three-component method for timely detection of land cover changes using polarimetric SAR images," *ISPRS J. Photogramm. Remote Sens.*, vol. 107, pp. 3–21, 2015.

[11] C. C. Freitas *et al.*, "Land use and land cover mapping in the Brazilian Amazon using polarimetric airborne P-Band SAR data," *IEEE Trans. Geosci. Remote Sens.*, vol. 46, no. 10, pp. 2956–2970, Oct. 2008.

[12] D. Lu, D. Li, E. Moran, L. V. Dutra, and M. Batistella, "A comparison of multisensor integration methods for land cover classification in the Brazilian Amazon," *GIScience Remote Sens.*, vol. 48, no. 3, pp. 345–370, 2011.

[13] G. Li, D. Lu, E. Moran, L. V. Dutra, and M. Batistella, "A comparative analysis of ALOS PALSAR l-band and radarsat-2 c-band data for land-cover classification in a tropical moist region," *ISPRS J. Photogramm. Remote Sens.*, vol. 70, pp. 26–38, 2012.

[14] V. Turkar, R. Deo, Y. Rao, S. Mohan, and A. Das, "Classification accuracy of multi-frequency and multi-polarization SAR images for various land covers," *IEEE J. Sel. Topics. Appl. Earth Observ. Remote Sens.*, vol. 5, no. 3, pp. 936–941, Jun. 2012.

[15] R. G. Negri, L. V. Dutra, and S. J. S. Sant'Anna, "An innovative support vector machine based method for contextual image classification," *ISPRS J. Photogramm. Remote Sens.*, vol. 87, pp. 241–248, Jan. 2014.

[16] D. G. Leckie, "Forestry applications using imaging radar," in *Principles and Applications of Imaging Radar: Manual of Remote Sensing*, vol. 2, 3rd ed., F. Henderson and A. Lewis., Eds. New York, NY, USA: Wiley, 1998, pp. 201–213.

[17] D. H. Hoekman and M. J. Quiriones, "Land cover type and biomass classification using AirSAR data for evaluation of monitoring scenarios in the Colombian Amazon," *IEEE Trans. Geosci. Remote Sens.*, vol. 38, no. 2, pp. 685–696, Mar. 2002.

[18] D. Lu *et al.*, "Land use/cover classification in the Brazilian Amazon using satellite images," *Pesquisa Agropecuaria Brasileira*, vol. 47, no. 9, pp. 1185–1208, 2012.

[19] S. R. Cloude and E. Pottier, "An entropy based classification scheme for land applications of polarimetric SAR," *IEEE Trans. Geosci. Remote Sens.*, vol. 35, no. 1, pp. 68–78, Jan. 1997.

[20] A. C. Frery, A. H. Correia, and C. C. Freitas, "Classifying multifrequency fully polarimetric imagery with multiple sources of statistical evidence and contextual information," *IEEE Trans. Geosci. Remote Sens.*, vol. 45, no. 10, pp. 3098–3109, Oct. 2007.

[21] J. S. Lee, D. L. Schuler, R. H. Lang, and K. J. Ranson, "K-distribution for multi-look processed polarimetric SAR imagery," in *Proc. Int. Geosci. Remote Sens. Symp. Surface Atmospheric Remote Sens., Technol., Data Anal. Interpretation*, vol. 4, 1994, pp. 2179 –2181.

[22] A. C. Frery, C. C. Freitas, and S. J. S. Santaanna, "Statistical characterization of SAR data: The multiplicative model and extensions," in *Proc. Simposio Latinoamericano de Percepción Remota*, 1995, pp. 502–515.

[23] C. C. F. Yanasse, A. C. Frery, and S. J. S. Sant'Anna, "Stochastic distribuition and the multiplicative model: Relation, properties, estimators and applications to SAR image analysis," National Institute for Space

Research, São José dos Campos, Brazil, *Tech. Rep. iNPE-5630-NTC/318*, 1995.

[24] A. Frery, H.-J. Muller, C. Yanasse, and S. Sant'Anna, "A model for extremely heterogeneous clutter," *IEEE Trans. Geosci. Remote Sens.*, vol. 35, no. 3, pp. 648–659, May 1997.

[25] J. S. Lee, K. Hoppel, S. Mango, and A. Miller, "Intensity and phase statistics of multilook polarimetric and interferometric SAR imagery," *IEEE Trans. Geosci. Remote Sens.*, vol. 32, no. 5, pp. 1017–1028, Sep. 1994.

[26] J. Besag, "On the statistical analysis of dirty pictures," *J. Roy. Stat. Soc.*, vol. B-48, pp. 259–302, 1986.

[27] R. Khedam, A. Belhadj-Aissa, and T. Ranchin, "Study of ICM parameters influence on images satellite contextual classification," in *Geoinformation for European-wide Integration*. Prague, Czech Republic: EARSEL, 2002, pp. 79–85.

[28] F. Bovolo and L. Bruzzone, "A context-sensitive technique based on support vector machines for image classification," in *Pattern Recognition and Machine Intelligence* (Lecture Notes in Computer Science), vol. 3776. Berlin, Germany: Springer, 2005, pp. 260–265.

[29] S. Theodoridis and K. Koutroumbas, *Pattern Recognition*, 4th ed. San Diego, CA, USA: Academic, 2008.

[30] H. Lin, C. Lin, and R. C. Weng, "A note on Platt's probabilistic outputs for support vector machines," *Mach. Learn.*, vol. 68, no. 3, pp. 267–276, 2007.

[31] R. G. Congalton and K. Green, *Assessing the Accuracy of Remotely Sensed Data*. Boca Raton, FL, USA: CRC Press, 2009.

[32] "Anomalias de precipitação - método dos quantis," Instituto Nacional de Meteorologia, Brasília, Brazil, 2016.

[33] "Global land survey," , U.S. Geological Survey, Sioux Falls, SD, USA, 2009.

[34] INPE. (2016). *Terraclass—Amazon land use database*. [Online]. Available: http://www.inpe.br/cra/projetos_pesquisas/terraclass.php

[35] W. B. Silva, C. C. Freitas, S. J. S. Sant'Anna, and A. C. Frery, "Classification of segments in PolSAR imagery by minimum stochastic distances between Wishart distributions," *IEEE J. Sel. Topics Appl. Earth Observ. Remote Sens.*, vol. 6, no. 3, pp. 1263–1273, Jun. 2013.

[36] J. S. Lee, L. Du, D. L. Schuler, and M. R. Grunes, "Statistical analysis and segmentation of multi-look SAR imagery using partial polarimetric data," in *Proc. Int. Geosci. Remote Sens. Symp. Quant. Remote Sens. Sci. Appl.*, vol. 2, 1995, pp. 1422–1424.

[37] C. Hsu, C. Chang, and C. Lin, "A practical guide to support vector classification," Dept. Comput. Sci., National Taiwan Univ., Taipei, Taiwan, *Tech. Rep.*, 2010.

[38] J. L. Jensen and J. Moller, "Pseudolikelihood for exponential family models of spatial point processes," *Annals Appl. Probab.*, vol. 1, no. 3, pp. 445–461, Aug. 1991.

Rogério Galante Negri received the graduated degree in mathematics from Universidade Estadual Paulista (UNESP), São José dos Campos, Brazil, in 2006, and the master and doctoral degrees (2013) in applied computing from Brazilian National Institute for Space Research, São José dos Campos, in 2006 and 2013, respectively.

His main research interests include pattern recognition and image processing. He is currently a Professor in the Environmental Engineering Department, UNESP.

Luciano Vieira Dutra was born in Sao Paulo, Brazil. He received the B.S.E.E degree, in 1976, from Aeronautical Technological Institute (ITA), São José dos Campos, Brazil, and the M.Sc. and Ph.D. degrees in computer science from the Brazilian National Institute for Space Research (INPE), São José dos Campos, in 1981 and 1989, respectively.

He was a Visiting Scholar at Sheffield University in 1991. Also, he went to the German Space Establishment (DLR) in 1995, 1997, and 1998, as a Visiting Scientist, to work with radar imagery information extraction. Since 1977, he has been with the INPE, where he is currently a Senior Researcher at the Image Processing Division. He has been working in several national and international large scale remote sensing projects. His research interests include SAR image processing, interferometry, pattern recognition, and remote sensing applications. He is also a Lecturer at INPE's Computer Science and Remote Sensing Graduate Programs, where he has been in charge of the Image and Signal Processing, Pattern Recognition, and Radar Image Processing Courses.

Corina da Costa Freitas received the B.S. degree in mathematics from the Pontifícia Universidade Católica de São Paulo in 1974, the M.Sc. degree in statistics from the Massachusetts Institute of Technology, Cambridge, MA, USA, in 1980, and the Ph.D. degree in statistics from the University of Sheffield, Sheffield, U.K., in 1992.

She is currently a Researcher at the Instituto Nacional de Pesquisas Espaciais, São José dos Campos, Brazil. Her research interests include statistical analysis of synthetic aperture radar (SAR) images and SAR image processing.

Dengsheng Lu received the B.A. degree in forestry from Zhejiang Forestry University, Hangzhou, China, in 1986, the M.A. degree in forestry from Beijing Forestry University, Beijing, China, in 1989, and the Ph.D. degree in physical geography from Indiana State University, Terre Haute, IN, USA, in 2001.

He is a Professor at Center for Global Change and Earth Observations, Michigan State University, East Lansing, MI, USA. He had worked at Indiana University Bloomington, Bloomington, IN, USA, as an Associate/Senior Scientist between 2008 and 2012 and as a Postdoctoral/Assistant Scientist between 2001 and 2006. He also had worked at Auburn University in 2007–2008 as a Research Fellow.His research interests include land-use/cover change, biomass/carbon estimation, human–environment interaction, and urban impervious surface mapping. He has published more than 90 peer-reviewed journal papers and 15 book chapters. His research projects are funded by NASA, NSF, NIH, and Brazilian CNPq.